



OPEN Study on freeze-thaw damage of surface and pore structure of steam cured concrete

Jialin Chen¹, Zhifan He², Shoukai Chen¹✉, Phu Minh Vuong Nguyen³, Jinping Liu¹ & Haoke Xu¹

The study of freeze-thaw (F-T) damage of steam cured concrete (SCC) plays a positive role in promoting the development of prefabricated technology in water conservancy project construction and construction industrialization in cold areas. This study aims to investigate and provide a better understanding of the surface damage pattern and pore structure of SCC. In this paper, a 3D scanner was used to scan the surface topography of SCC under five conditions of F-T (the number of F-T was 0, 50, 100, 150, and 200 respectively), and the spatial distribution of point cloud data generated by scanning results was analyzed, and surface roughness was introduced to quantify the damage effect of F-T cycle on the surface of SCC. The results show that the fluctuation range of point cloud data increases from 0–0.15 mm to 0–0.93 mm with the increase of F-T cycles. The F-T cycles result in the continuous deterioration of the surface of SCC, and surface roughness increases from 0.097 mm to 0.899 mm, and the development law basically conforms to the exponential growth law. In addition, the pore structure parameters of SCC under different F-T cycles were obtained based on X-ray computed tomography technology (XCT). It was found that the pore size and porosity increased with the increase of F-T cycles, and the growth rates ranged from 3.41% to 19.69% and 29.29% to 41.85%, respectively. The pore numbers showed a decreasing trend, with the decreasing rate ranging from 2.56% to 11.56%. It is also found that the inhomogeneity of pore space distribution caused by F-T cycles may be one of the main reasons affecting the mechanical properties of SCC. On this basis, the surface fractal dimension and volume fractal dimension of SCC pores were calculated respectively, and they were used to evaluate the F-T damage degree of SCC under different F-T cycles. The results revealed that there is a linear relationship between fractal dimension and F-T cycles. When the fractal dimension is used to characterize the F-T damage degree of SCC, the result of the volume fractal dimension is better than the surface fractal dimension.

Keywords Steam cured concrete, Freeze-thaw damage, Surface roughness, Pore structure, Fractal dimension

In recent years, precast concrete elements have begun to be promoted and applied in the field of water conservancy and water transportation with the rapid development of green buildings and prefabricated buildings. For example, precast aqueduct¹, prefabricated precast revetment and prefabricated slope retaining pile², etc. The quality of concrete, demolding speed and mold turnover are all related to the benefit and safety of elements³. Steam curing is one of the main methods for elements⁴, and it mainly changes the curing environment of concrete by means of high temperature humidification, so that the hydration reaction of cement is advanced and accelerated, thereby improving the early strength of concrete and achieving the purpose of improving production efficiency⁵.

Due to the difference in geographical location and climatic environment, F-T cycles are a phenomenon that frequently occurs in some regions. Throughout their service life, F-T cycles may harm SCC to differing degrees⁶. On the one hand, SCC will be subjected to the action of the thermal and moisture coupling effect in the curing process⁷, resulting in certain initial damage to its surface⁸. The F-T cycle makes the surface of SCC more susceptible to F-T damage compared to ordinary concrete. On the other hand, the thermal and moisture coupling effect will degrade and coarsen the pore structure of SCC⁹, while the volume difference of F-T media caused by F-T cycles will further damage the pore structure of SCC¹⁰. This combined external and internal damage mechanism is particularly prominent in water conservancy projects in cold regions. The sustained F-T conditions created by low-temperature water-exposed environments not only cause surface spalling, mass

¹North China University of Water Resources and Electric Power, Zhengzhou 450046, China. ²Henan Industrial School, Zhengzhou 450003, China. ³Central Mining Institute-National Research Institute, 40166 Katowice, Poland. ✉email: Man200177@163.com

loss, and performance degradation of SCC, but also accelerate the overall deterioration process of the material through the destruction of the pore structure. This ultimately leads to shortened service life and even instability or failure of engineering structures, posing serious threats to their safety^{11,12}. Therefore, it is very important to accurately quantify and reveal the changes and regularities of the surface and pore structure of SCC in the F-T environment.

3D scanner technology records the geometric structure and appearance of scanned objects with lasers and high-speed cameras¹³, constructs 3D images of scanned objects through mathematical modeling with computer technology, and then analyzes and measures 3D digital models in a computer environment¹⁴. And this technology has been widely used in the field of concrete. For example, several studies^{15–17} studied the influences of different aggregate types, nozzle size, printing path, and other printing parameters on the performance of 3D printed concrete based on 3D scanner technology. The literature¹⁸ studied the application of concrete based on 3D scanning technology for F-T tests under different aggregate substitution rates. The literature¹⁹ studied the 3D surface roughness parameters of concrete based on 3D scanner technology, and established the correlation between the parameter and the tensile adhesion of concrete. The literature²⁰ tested the surface roughness of concrete based on the 3D scanner technology of single camera, and believed that the cost of this technology was low, but the accuracy was not affected. For example, the overall mean error of surface roughness is less than 3%, and the local mean error is less than 5%. The above research shows that using 3D scanner technology to measure and analyze the surface of concrete has high precision and operability.

XCT is a powerful tool to investigate the concrete pore structure^{21–23}. It has the characteristics of non-destructive and repeatable operation compared with mercury intrusion porosimetry, scanning electron microscope, optical microscope, and other equipment^{24–26}. Moreover, it is especially suitable for the testing the same sample under different working conditions. The literature²⁷ studied the pore structure changes of mortar before and after F-T based on XCT. Cracks and filling of pores caused by the F-T cycle can be obtained by comparing the pore structure of the same test specimen before and after F-T. The literature²⁸ continuously observed the pore structure of concrete with F-T cycles of 25, 50, 75, and 100 based on XCT, and found that the pore area distribution of concrete gradually increased with the increase of F-T cycles, and accompanied by cracks. The literature²⁹ obtained the evolution process of glass concrete pore structure under the two mixing processes of dry mixing and wet mixing via XCT. It is believed that XCT is better than mercury intrusion porosimetry in studying concrete pore structure under the dry mixing process. The literature³⁰ used XCT to test the pore structure parameters of foam concrete and the correlation between pore structure and early mechanical properties was clarified. The above literature proves the feasibility of using XCT to study the pore structure evolution of SCC under F-T cycles. However, although the pore structure of SCC can be characterized by XCT, there are many parameters of the pore structure³¹. It is bound to complicate and difficult to quantify the F-T damage of SCC if the pore structure parameters are directly used to judge the F-T damage³². The introduction of fractal theory provides a powerful mathematical tool for solving this challenging problem. Its core advantage lies in utilizing the fractal dimension—a non-integer dimension—to quantitatively characterize the self-similarity or statistical similarity of pore structures under scale transformations. This effectively captures the complexity of pore structures. Therefore, it is necessary to describe the pore structure of SCC with the help of fractal theory³³, so as to quantify the F-T damage of SCC.

At present, the evaluation of F-T damage in SCC mainly refers to ordinary concrete, using indicators such as visual observation of surface spalling degree, core sampling for mass loss measurement, and relative dynamic elastic modulus. This approach has limitations such as large result dispersion due to strong subjectivity, destruction of samples, inability to conduct repeated observation, and lack of capability to track local damage evolution. Based on this, this paper will introduce 3D scanner and XCT technologies to conduct a quantitative study on the F-T damage of SCC through non-destructive means. First, the surface of SCC samples under different numbers of F-T cycles will be scanned using a 3D scanner, and surface roughness will be adopted to quantify the surface damage caused by F-T cycles to SCC. Second, XCT will be used to test the pore structure of SCC under different F-T cycles, aiming to study the evolution laws of pore parameters such as pore size distribution, pore number, and porosity. Finally, on the basis of studying the pore structure of SCC, the surface fractal dimension and volume fractal dimension of the pore structure will be calculated respectively, and fractal dimensions will be utilized to characterize the F-T damage of SCC.

Materials and methods

Material properties

The cement was P-O 42.5 ordinary Portland cement with specific surface area of 348.70 m²/kg, and the specific parameters were shown in Table 1. The coarse aggregate was natural crushed stone with a continuous grading of 5–25 mm; The fine aggregate was a natural medium river sand with a fineness modulus of 2.5. The mineral admixture was fly ash (FA) and ground granulated blast furnace slag (GGBS), whose specific chemical compositions were shown in Table 2; The water reducing agent was a high-efficiency polycarboxylic acid water reducing agent with a water reduction rate of 28% and an air content of 2.5%.

MgO/%	SO ₃ /%	Ignition loss /%	Cl ⁻ /%	f _v /MPa(3d/28d)	f _{ct} /MPa(3d/28d)	Initial setting time /min	Final setting time /min
5.0	3.5	5.0	0.06	16/42.5	3.5/6.5	45	600

Table 1. Main indexes of cement.

Materials	Class	SiO ₂ /%	Al ₂ O ₃ /%	Fe ₂ O ₃ /%	CaO/%	MgO/%	SO ₃ /%
FA	II	56.63	24.82	6.85	3.36	/	/
GGBS	S95	34.01	9.85	1.02	41.87	8.11	2.67

Table 2. Chemical composition of FA and GGFS.

Cement	FA	GGBS	Water reducing agent	Coarse aggregate	Sand	Water	W/B
241.5	144.9	96.6	3.42	957	815	145	0.3

Table 3. Experiment mixes proportion (kg/m³).

Experiment mix proportion

The experimental mix proportion design was shown in Table 3.

Steaming system and preparation process

The experiment used an SJD60 single-horizontal-shaft forced concrete mixer. First, half of the water and aggregates were placed in the mixer and stirred for 3 min. Next, the remaining water, cement, and water-reducing agent were added and stirred for 2 min. Then, river sand was added and stirred for 2 min. Finally, GGFS and FA were added and stirred for 2 min. The mixture was compacted by vibration on an HZD1000 concrete testing vibration table for 20 s, then cured under natural conditions for 3 h before transfer to a steam curing chamber. Steam curing lasted 12 h at 40 °C with a heating rate of 15–20 °C/h. After steam curing, the concrete samples were placed in a standard curing room for 28d. The specific process is shown in Fig. 1.

Test methodology

The F-T cycle test

The F-T cycle test of SCC refers to GB / T 50,082 – 2024³⁴ and ASTM C666³⁵, and was completed by a CABR-HDK rapid F-T cycles testing machine produced by China Jianyanhuace Measuring Instrument Co., Ltd. The F-T cycle test was carried out according to the following principles: the specimens were frozen in a F-T equipment with an air temperature of -18 °C for 2 h, and the specimen were thawed by injecting water at 20 °C for 2 h. A F-T cycle was 4 h, and the test period had a total of 200 F-T cycles. The F-T cycles medium is -45 °C antifreeze, the refrigeration compressor is 5 HP, the F-T cycles mechanical voltage is AC 380 V, the current change is 50 cycles/s, the heating power is 9 KW, and the maximum operating power is 9.85 KW. The total number of F-T cycles is 200, and the duration of each F-T cycles is 4 h. In order to accurately characterize the destructive effects of the F-T environment on SCC, F-T cycling, 3D scanning, and XCT were performed on the same cube specimen with a size of 50 × 50 × 50 mm.

3D scanner

(1) Device parameters.

The scanner is a four-eye 3D scanner produced by China Nanyang Mengyang Machinery Co., Ltd. The scanning mode is blue light plus white light dual mode. The scanning accuracy is 0.001 to 0.05 mm. The number of points in a single amplitude scan is 2,600,000 pixels. The single face scan speed is 1 to 3 s. The average point spacing is 0.005 to 0.1 mm. The working voltage is 220 V. The operating temperature is from -20 °C to 40 °C. Test frequency is 100 F-T cycles / time.

(2) Point cloud data processing.

Point cloud data processing generally includes point cloud data denoising, point cloud data simplification, point cloud data stitching and defect repair, etc.^{36–38}. Specimen surface roughness and surface splicing errors probably occur in the process of 3D digital model reconstruction, because there are many interferences and uncontrollable information in the scanning process, such as scanning environment and neighboring objects³⁹. Therefore, denoising should be carried out by eliminating interference information and applying filtering in the process of point cloud data, and bilateral filtering denoising method is adopted in this case⁴⁰.

The 3D scanner needs to obtain a large number of point cloud data to ensure the ac-curacy of the surface information of SCC. However, in order to improve the convenience of large point cloud data storage and computing, point cloud data needs to be streamlined. Its principle is generally as follows: some representative point cloud data are selected to reconstruct the 3D digital model of the surface topography of SCC under the condition that various 3D characteristic information of the surface of SCC is not missing⁴¹.

Due to the 3D nature of SCC samples, single scans inevitably produce blind spots. Therefore, during scanning, the spatial invariance of marker points must be utilized with a high-precision electric rotating stage. By fixing the scanner position and scanning angle, overlap of marker points between adjacent viewpoints is ensured, enabling 3D reconstruction of the SCC surface from multiple perspectives. 3D point cloud automatic splicing algorithm is adopted to splice the extracted obvious feature points on the surface of SCC in this paper⁴². Data loss will occur during surface point cloud data acquisition of SCC, because the data quality will be limited by measurement

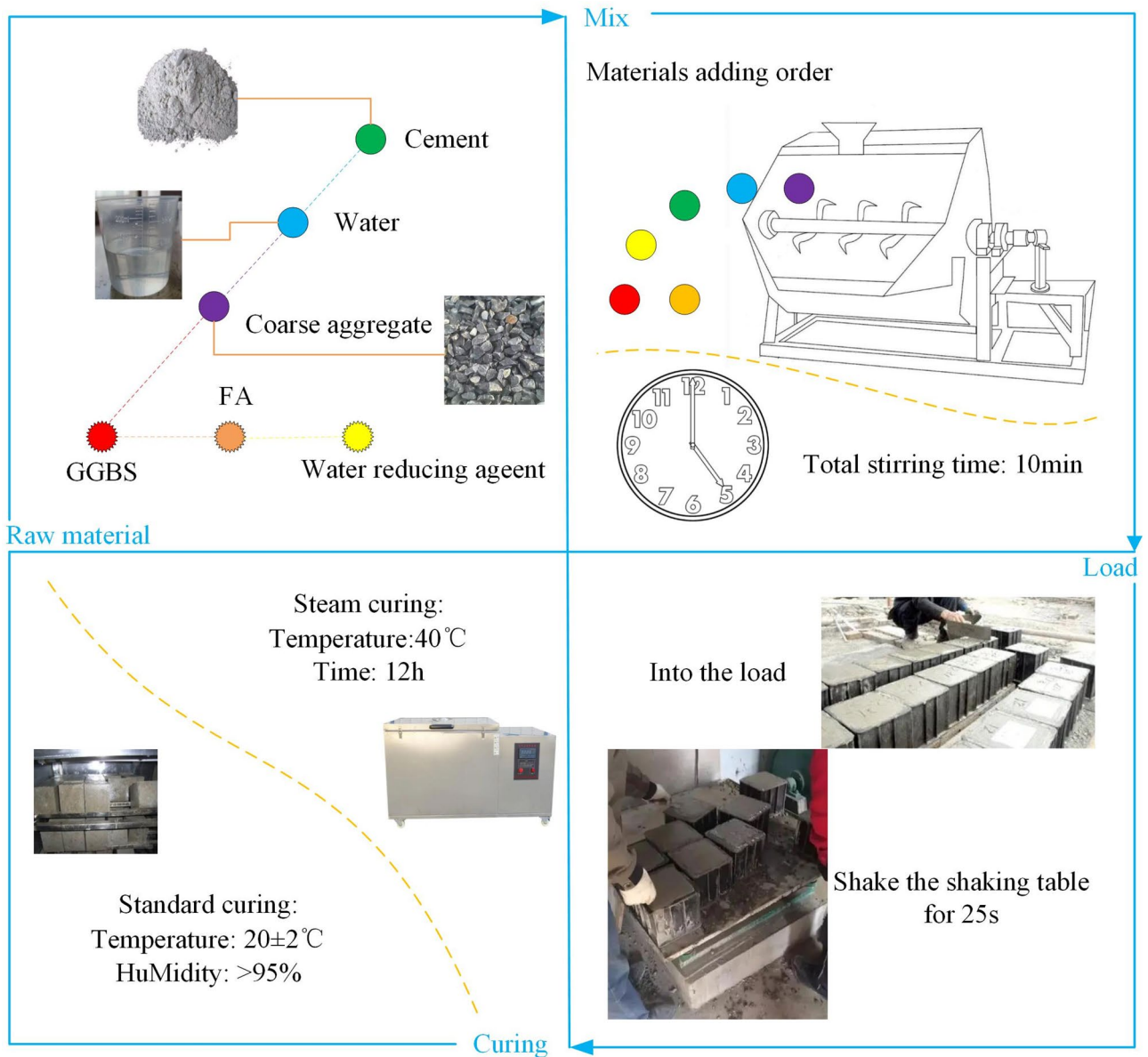


Fig. 1. Flow chart of SCC preparation.

equipment and methods, as well as the paste of marker points and defects on the surface of solid model. On the other hand, the effect of the geometric processing algorithm is also affected by model quality. Therefore, it is necessary to repair the missing data in order to apply it robustly to the subsequent digital geometry processing. This paper adopts a content-based point cloud model repair method⁴³.

(3) Reconstruction of 3D digital model.

The surface of SCC was extracted by a 3D scanner, and the point cloud data was processed respectively according to the above steps. In addition, we also scanned the corners of the SCC in order to make the splicing of the surface of the SCC stronger. The 3D reconstruction of point cloud data is realized by splicing surfaces, edges, and corners based on the automatic splicing algorithm. The result of the 3D reconstruction is shown in Fig. 2.

XCT

(1) Device parameters.

The pore structure characteristics of SCC were analyzed by the German Y. CT Precision microfocus X-ray and industrial CT system, which is mainly composed of X-ray source, rotating console, and monitor. The spatial resolution of the scanned image is 78.4 μm / voxel, and the pixel number is 1024 \times 1024; the length resolution is 37.4 μm . Test frequency is 50 F-T cycles / time.

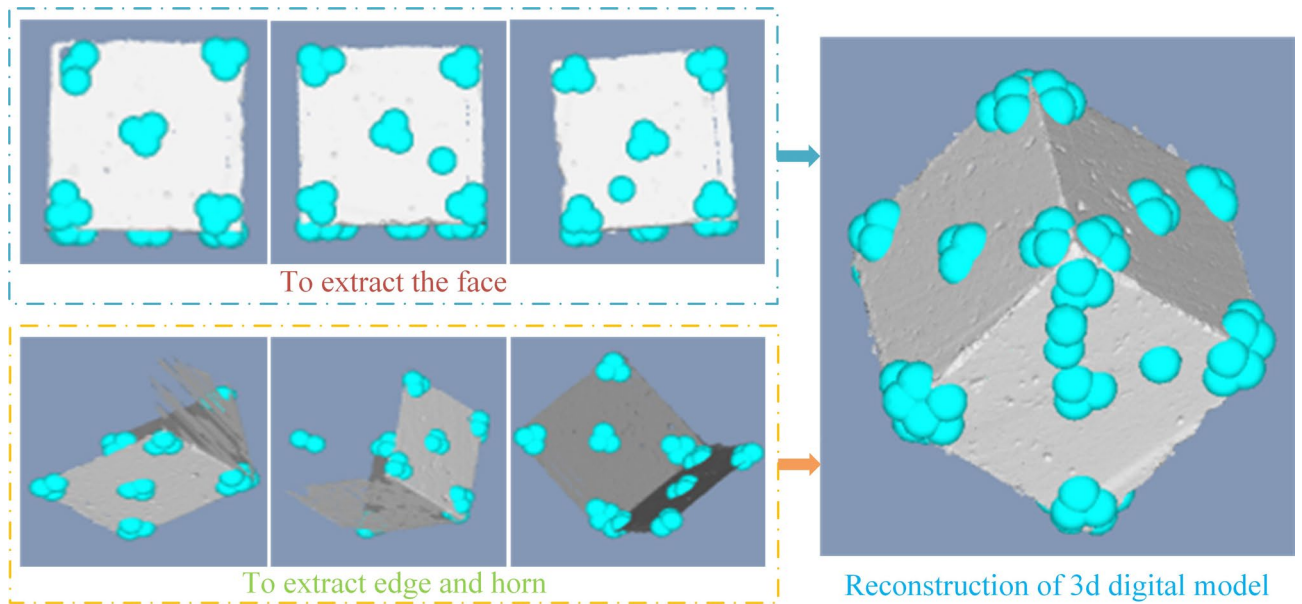


Fig. 2. 3D reconstruction of point cloud data.

(2) Denoise processing.

Denoising processing solves the beam hardening problem by cutting the SCC 2D slices^{44,45}. As digital images will be interfered by imaging equipment and external environmental noise during digitization and transmission, it is necessary to de-noise the image⁴⁶. Some studies have shown that the non-local mean method has the best noise reduction effect⁶, so the non-local mean noise reduction method is selected in this paper.

(3) Grayscale division.

There are significant differences in X-ray penetration due to the differences in aggregates, cement mortar thickness, and pores of SCC. On the basis of eliminating beam hardening and reducing image noise, ImageJ software (v1.8.0) is used to determine the grayscale range of 2D slices of SCC, in order to accurately segment the grayscale of aggregates, cement mortar, and pores of SCC. Among them, the gray value range of pores is 0–13,597, the gray value range of cement mortar is 13,597–16,804, and the gray value range of aggregates is 16,804–23,056.

(4) 3D reconstruction of SCC.

A total of 1000 2D slices were processed by Avizo software (2019 version). Aggregates, cement mortar, and pores were extracted according to the results of grayscale division, and 3D reconstruction of SCC was carried out. The 3D reconstruction results are shown in Fig. 3.

Results and discussion

Analysis of the influence of F-T environment on the surface of SCC

Surface topography of SCC under F-T environment

There may be placement problems with the F-T test machine for SCC. In other words, SCC specimens may come into contact with F-T containers or other specimens in the same group during the test. Therefore, we selected a group of SCC surfaces that are only in contact with F-T liquid. The purpose of doing this is to obtain a more realistic F-T effect and reduce measurement errors.

Figure 4 shows the surface topography of SCC after 0, 50, 100, 150, and 200 F-T cycles. It can be seen from the figure that the surface of SCC has different degrees of damage even without F-T cycles. This is mainly due to the action of the thermal and moisture coupling effect on SCC during steam curing⁷. The surface damage of SCC tends to deteriorate with the increase in F-T cycles, which is basically consistent with the phenomena observed in ordinary concrete.

Spatial distribution of point cloud data

The steps and methods in Section “3D scanner” were used to scan the surface of SCC under different F-T cycles. Point cloud data after scanning are spatial coordinate points with 3D characteristics. Since only the F-T characteristic surface of SCC is discussed in this paper, it is assumed that the length and width of the SCC specimen do not change during F-T cycles, i.e., the F-T environment only affects the depth (height) of the SCC surface.

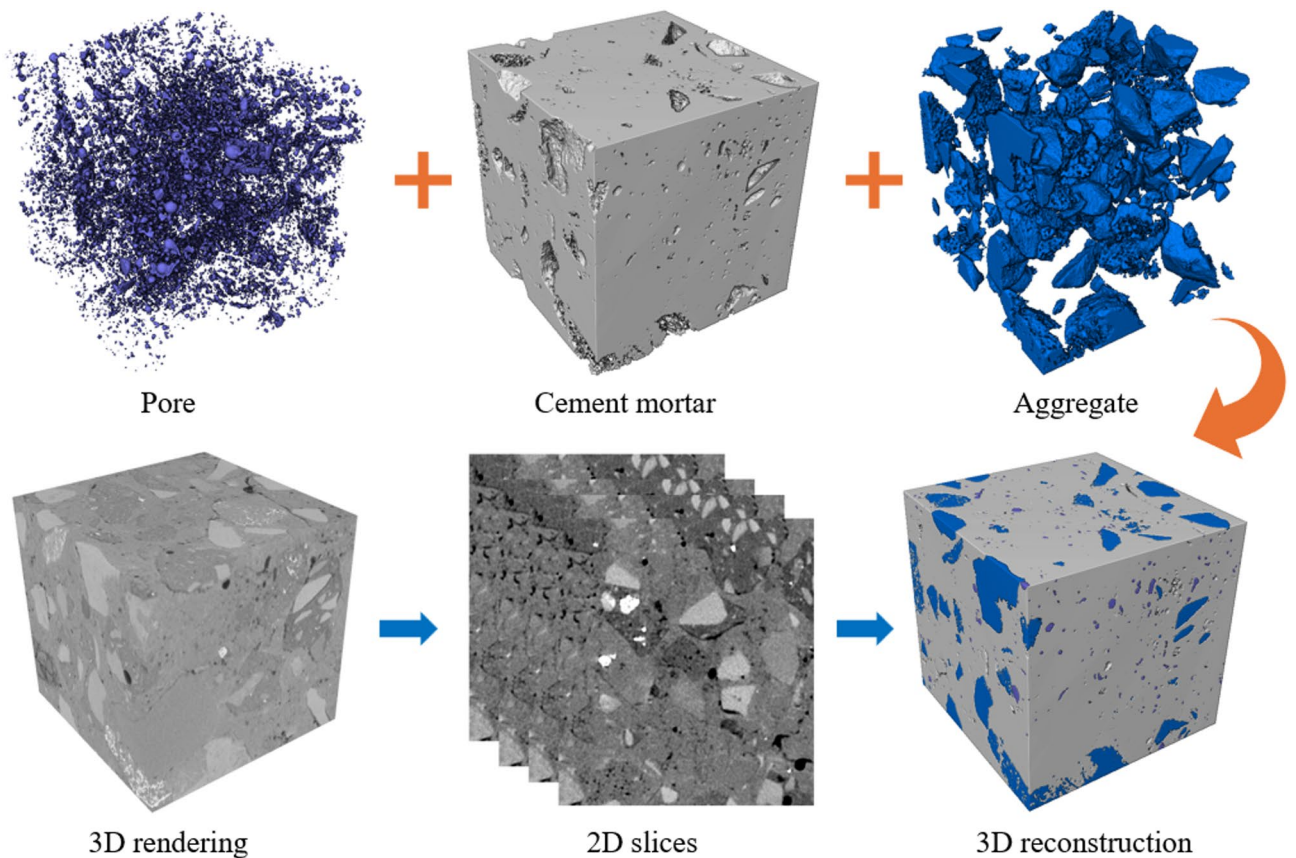


Fig. 3. 3D reconstruction of SCC.



Fig. 4. Surface topography of SCC under different F-T cycles.

Figure 5 shows the point cloud distribution of the surface F-T depth of SCC after 0, 50, 100, 150, and 200 F-T cycles. It can be seen that the fluctuation range of point cloud data gradually increases with the increase in F-T cycles. The point cloud data fluctuate between 0 and 0.15 mm, and most point clouds are located at 0 when no F-T cycles are applied. This indicates that the surface of SCC remains flat, even though affected by the steam curing system. The fluctuation ranges of point cloud data are 0–0.36 mm, 0–0.54 mm, 0–0.77 mm, and 0–0.93 mm when the number of F-T cycles increases to 50, 100, 150, and 200. It can be seen that the maximum value of the point cloud data range exhibits a growing trend, with growth rates of 0.16%–0.23% under different F-T cycles.

Calculation of surface roughness

In this paper, a physical evaluation index for concrete joint surface, namely surface roughness, is introduced to quantify the influence of F-T cycles on the surface of SCC. Methods for calculating surface roughness include the standard plate comparison method, the sand-patch method, and the probe method, etc.⁴⁷. Based on the principle of the sand-patch method⁴⁸, coordinated adjustment and filling were carried out on the spatial distribution of

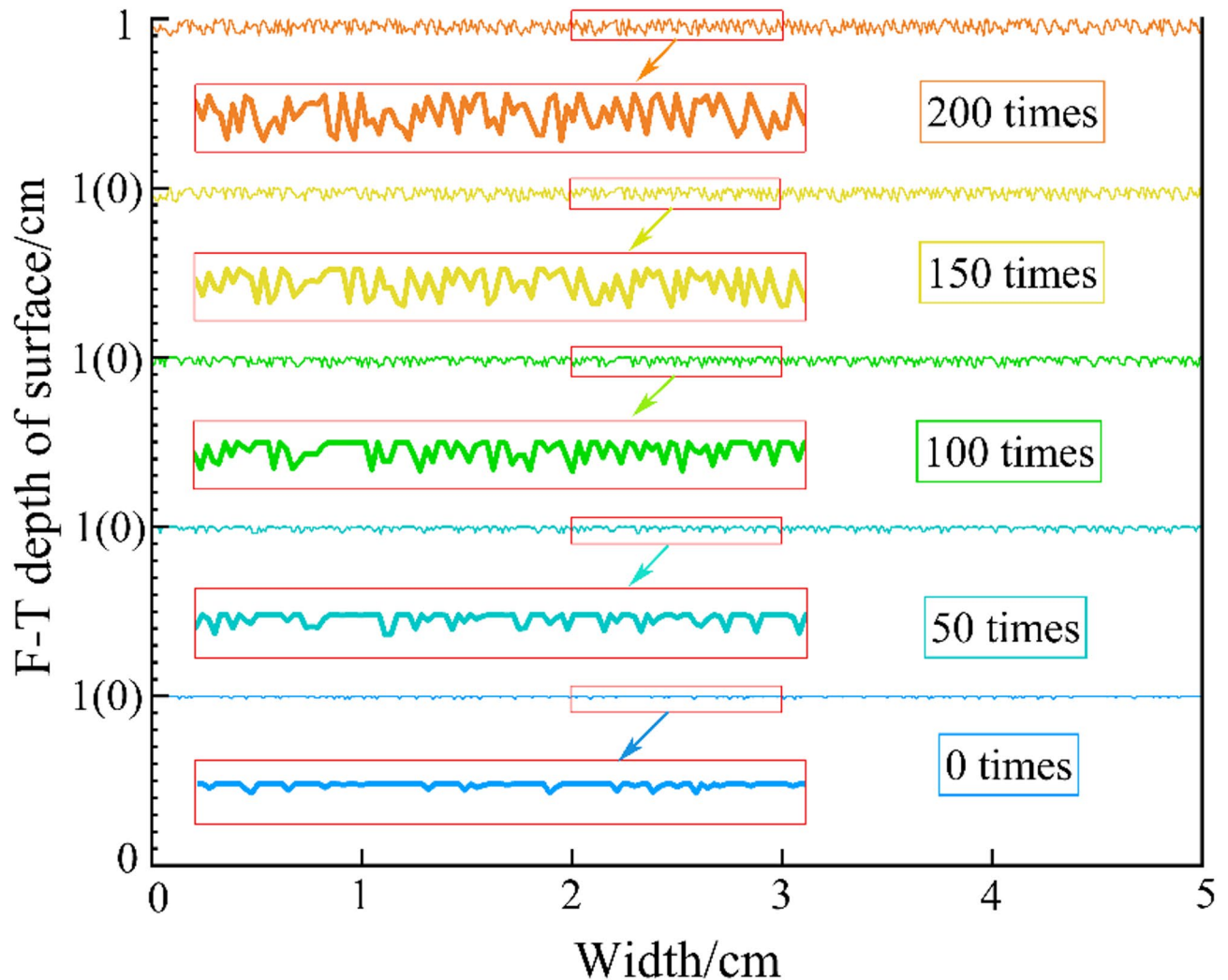


Fig. 5. Point cloud distribution of surface F-T depth of SCC.

extracted point cloud. Mass and density were given to the filled body, and the volume and area covered by the filled body were calculated respectively, so as to obtain the surface roughness of SCC after different F-T cycles.

Figure 6 shows the surface roughness of SCC after 0, 50, 100, 150, and 200 F-T cycles. It can be seen that the surface roughness of SCC increases continuously with the increase in F-T cycles. For example, the surface roughness of SCC is 0.097 mm when there are 0 F-T cycles. The surface roughness of SCC is 0.137, 0.226, and 0.383 mm when the number of F-T cycles increases to 50, 100, and 150. These values increase by 1.41, 2.33, and 3.95 times compared with 0 F-T cycles, respectively. It can be seen that the surface roughness of SCC increases about 4 times when 150 F-T cycles are applied. This is due to water going through the freezing-thawing cycle during F-T exposure, resulting in a volume difference of about 9 times between liquid and solid water. SCC specimens begin to shed large areas of mortar debris when the phase change tension generated by F-T cycles exceeds that of the SCC pore structure⁴⁹, resulting in a sudden increase in surface roughness. In addition, it is worth noting that the surface roughness changes dramatically, with its value reaching as high as 0.899 mm when the number of F-T cycles is 200. The surface roughness increases by 9.27 times compared to 0 F-T cycles. At this stage, the surface of SCC begins to shed large particles such as river sand with large particle size or coarse aggregate with small particle size, and the surface is almost completely destroyed, accompanied by cracks.

The model Exp3P2 was used to fit the surface roughness of SCC according to the calculation results. It is found that R^2 reaches 0.998 when $a = -2.27$, $b = 3.31 \times 10^{-3}$, and $c = 3.74 \times 10^{-3}$. Therefore, we believe that the surface roughness of SCC under 0, 50, 100, 150, and 200 F-T cycles follows the exponential growth law. In addition, the mass loss rate and the relative dynamic elastic modulus of SCC were tested when the number of F-T cycles is 200. It is found that the mass loss rate of SCC is less than 5%, and the relative dynamic elastic modulus is more than 60%⁵⁰. This indicates that F-T damage had not completely occurred at this stage. Therefore, the Exp3P2 model can be used to predict the surface roughness of SCC under subsequent F-T cycles.

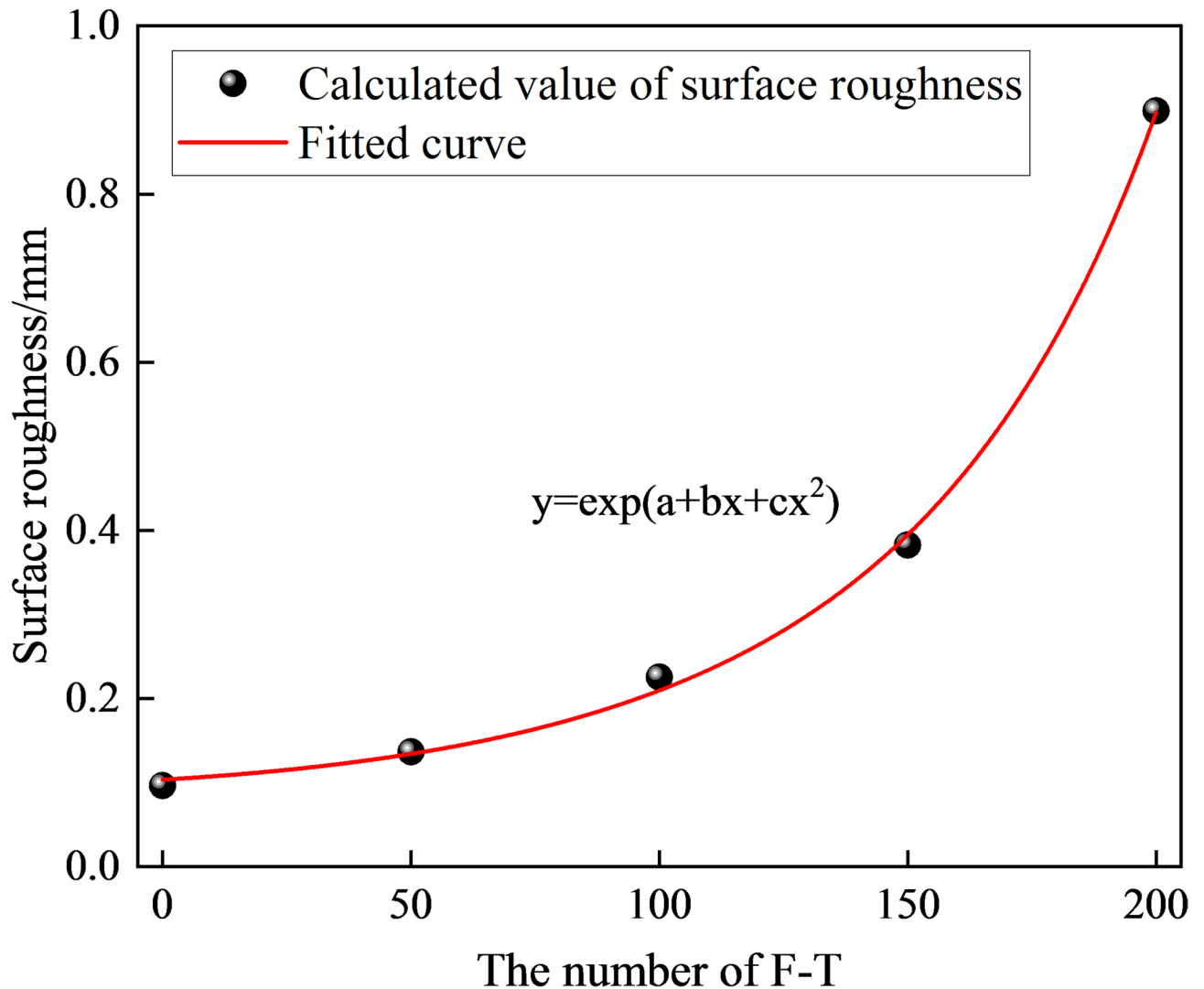


Fig. 6. Surface roughness and fitting curve of SCC under different F-T cycles.

Analysis of influence of F-T cycles on pore structure of SCC

The pore structure of SCC generally includes pore size distribution, the number of pores, and porosity, etc⁵¹. In order to understand the influence of F-T cycles on the pore structure characteristics of SCC, the pore structure parameters of SCC after 3D reconstruction were quantitatively characterized according to the steps in Section “XCT”.

Pore size distribution and pore numbers

Figure 7; Table 4 show the graph of the pore size distribution and pore structure parameters of SCC after 0, 50, 100, 150, and 200 F-T cycles, respectively. It can be seen that the pore size of SCC increases with the increase in F-T cycles. The maximum pore size range of SCC increases from 1095.68 μm to 1134.31 μm , 1302.25 μm , 1601.33 μm , and 1993.82 μm when the number of F-T cycles is 0, 50, 100, 150, and 200, respectively, and the growth rates are 3.41%, 12.90%, 18.68%, and 19.69%, respectively. The reason for this phenomenon is analyzed, and it is believed that the conversion between liquid phase and solid phase in the F-T cycles process will produce frost heaving force⁵², which continuously exerts tension on the pore structure⁴⁹, leading to the continuous increase of pore size. In addition, it is worth noting that the minimum pore size of SCC is 17 μm , which depends on the resolution of XCT.

In addition, Fig. 7; Table 4 visually show the influence of F-T cycles on the number of pores of SCC. The number of pores is 21,147, 19,908, 19,399, 17,265, and 15,269 when the number of F-T cycles is 0, 50, 100, 150, and 200, respectively. It can be seen that the number of pores of SCC decreases with the increase in F-T cycles. This is due to the fact that the pores of SCC will fuse with the surrounding pores to form larger pores when the pores are damaged by F-T cycles⁵³. This conclusion can also be verified in the pore size distribution mentioned above.

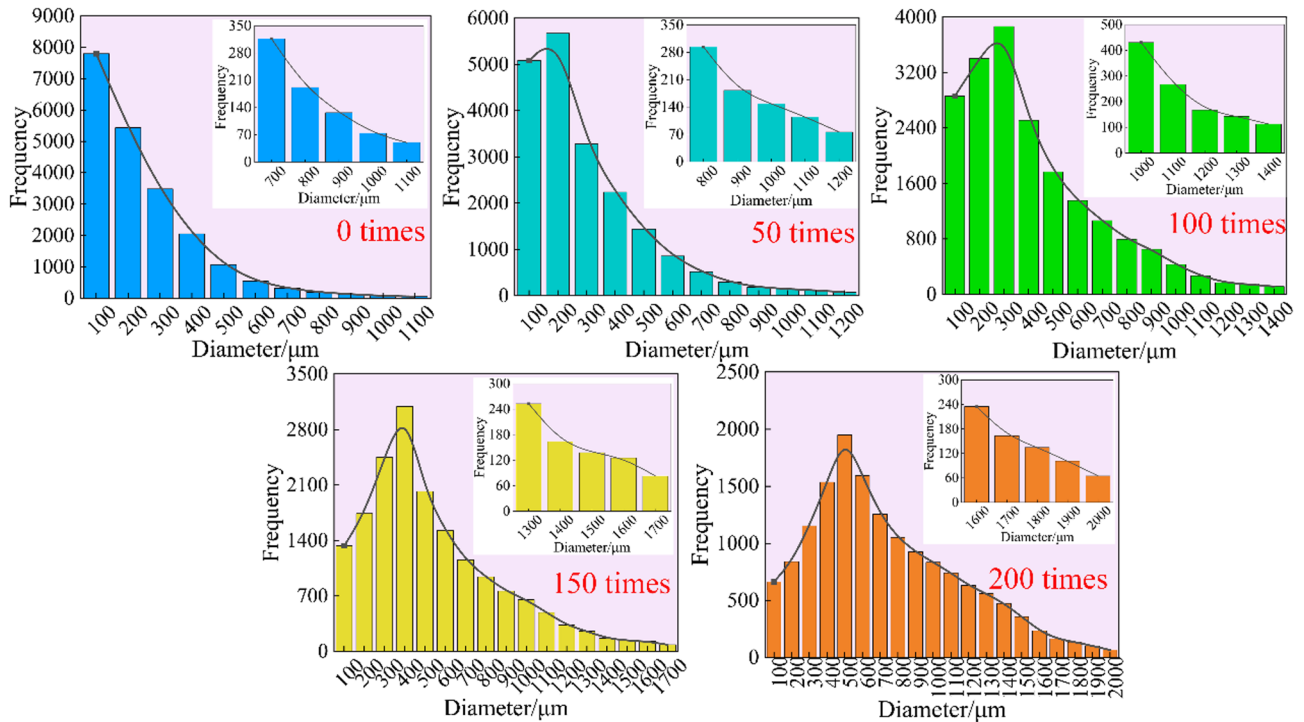


Fig. 7. Pore size distribution of SCC under different F-T cycles.

F-T cycles	Maximum pore size	Minimum pore size	Average pore size	Number of pores
0	1095.68	72.95	17	21,147
50	1134.31	73.03	17	19,908
100	1302.25	73.94	17	19,399
150	1601.33	77.25	17	17,265
200	1993.82	84.54	17	15,269

Table 4. Pore structure parameters of SCC (μm).

Porosity and pore Spatial distribution

In order to understand the influence of F-T cycles on the porosity of SCC, the chart of pore spatial distribution was drawn, as shown in Fig. 8. It can be seen from the figure that the porosity and its range of SCC show an increasing trend with the increase in F-T cycles. For example, the porosity of SCC is 1.25%, 1.89%, 3.25%, 4.66%, and 6.59%, respectively, when the number of F-T cycles is 0, 50, 100, 150, and 200, and the growth rates are 33.86%, 41.85%, 30.26%, and 29.29%. At this time, the porosity ranges of SCC are 0.77%–1.96%, 1.32%–3.5%, 2.60%–5.30%, 3.18%–9.16%, and 4.18%–15.32%, respectively. It can be seen that the pore spatial distribution is relatively stable when the number of F-T cycles is 0. The pore spatial distribution fluctuates greatly when the number of F-T cycles increases to 50, 100, 150, and 200, respectively. This is due to the merging and fusion of pores in the SCC during F-T cycles⁵³. This may be one of the main reasons affecting the mechanical properties of SCC, because the inhomogeneity of pore space distribution will change the stress distribution of SCC during loading. In addition, the inhomogeneity of pore space distribution is also helpful to estimate the damage location of SCC⁴⁴.

At the same time, we also found that the porosity of surface layer slices of SCC shows an explosive growth trend with the increase in F-T cycles, and the greater the number of F-T cycles, the deeper the surface layer slices are affected by F-T cycles. For example, the slice depth affected by F-T cycles is about 15 μm when the number of F-T cycles increases from 0 to 50; when the number of F-T cycles continues to increase to 100, 150, and 200, the affected slice depth increases to about 25, 45, and 80 μm , respectively. This is mainly caused by the F-T cycles developing from the outside to the inside⁵⁴. The porosity of the surface layer shows a trend of gradual increase when the SCC begins to be affected by F-T cycles, and the F-T cycles will further affect the deep surface layer of SCC when the pores on the surface layer merge or fuse due to frost heaving damage⁵⁵.

F-T damage degree analysis based on fractal dimension

Due to the large number of pore structure parameters of SCC, they show different development laws with the increase in F-T cycles. For example, the pore size distribution and porosity of SCC increase with the

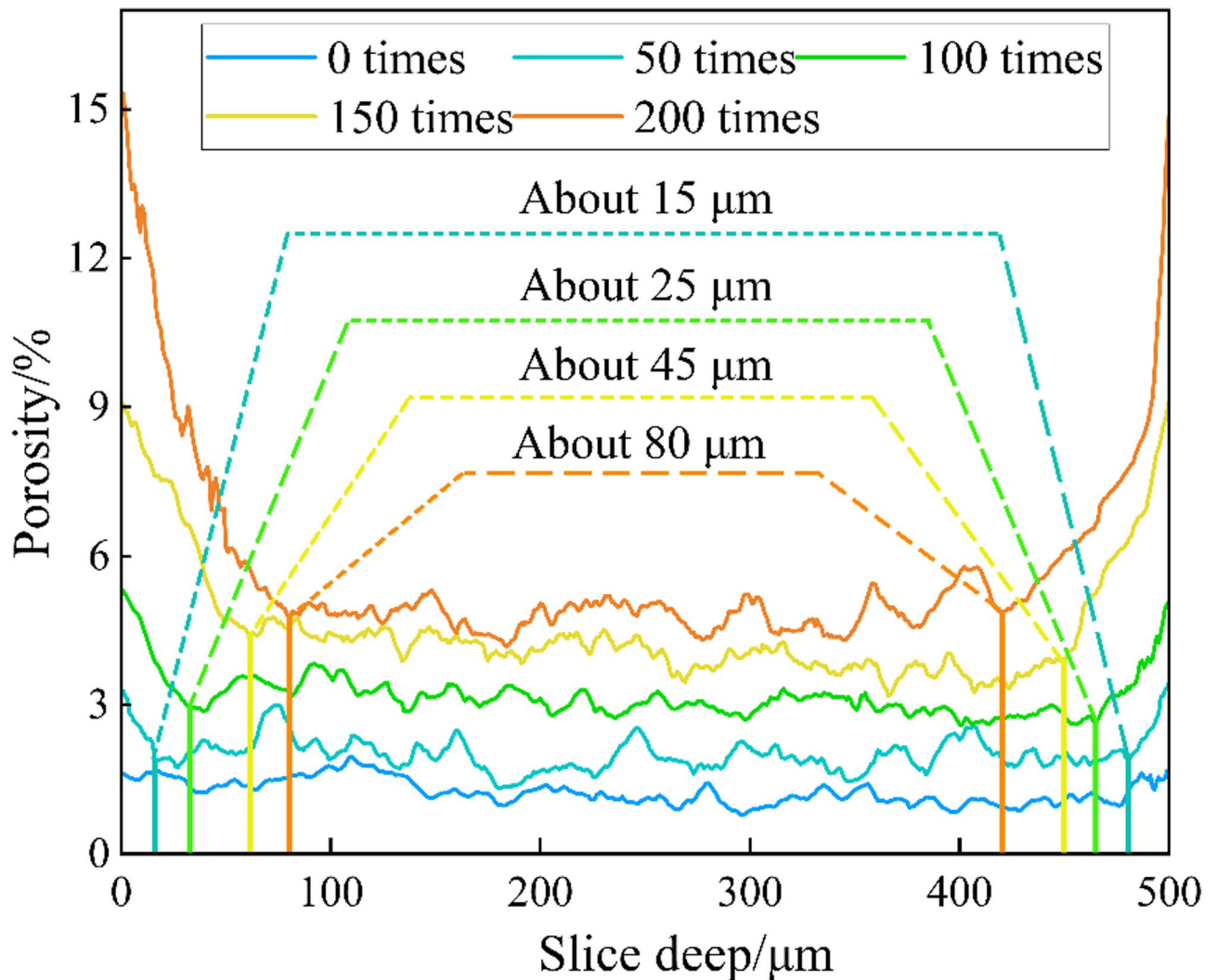


Fig. 8. Pore space distribution of SCC under different F-T cycles.

increase in F-T cycles, while the number of pores decreases with the increase in F-T cycles in Section “[Pore size distribution and pore numbers](#)” and “[Porosity and pore spatial distribution](#)”. Therefore, it is necessary to use fractal dimension to describe the pore structure parameters of SCC before and after F-T cycles⁵⁶. Existing studies show that fractal dimension can effectively characterize the pore structure of porous materials such as concrete and rock^{51,57}, and using fractal dimension as the basic parameter for pore structure analysis can establish a close correlation with the macroscopic properties of materials⁵⁸. However, most researchers focus on the surface of pores in fractal dimension studies, which seems to pay insufficient attention to pore volume⁴⁴. The concrete surface is easily affected by external environmental factors, which affect the measurement results of the surface fractal dimension, resulting in the inability to accurately reflect the degree of frost damage. The volume fractal dimension can reflect the structural characteristics of the entire internal space of concrete, including the distribution and complexity of pores and cracks in three-dimensional space^{59,60}. Therefore, the surface fractal dimension and volume fractal dimension of the pore structure of SCC were calculated in this paper under different F-T cycles. The results are shown in Fig. 9.

As can be seen from Fig. 9, both surface fractal dimension and volume fractal dimension of SCC pores show a decreasing trend with the increase of F-T cycles, and their ranges were 2.307–2.366 and 3.055–3.187, respectively. The surface fractal dimension and volume fractal dimension of SCC pores and the 0, 50, 100, 150, and 200 F-T cycles were fitted by the MATLAB fitting toolbox. It was found that there was a linear correlation between surface fractal dimension, volume fractal dimension and F-T cycles, and the R^2 values were 0.988 and 0.976.

According to Lemaitre and Kochanov definition of damage variables^{61,62}:

$$D = 1 - \frac{\tilde{A}}{A} \quad (1)$$

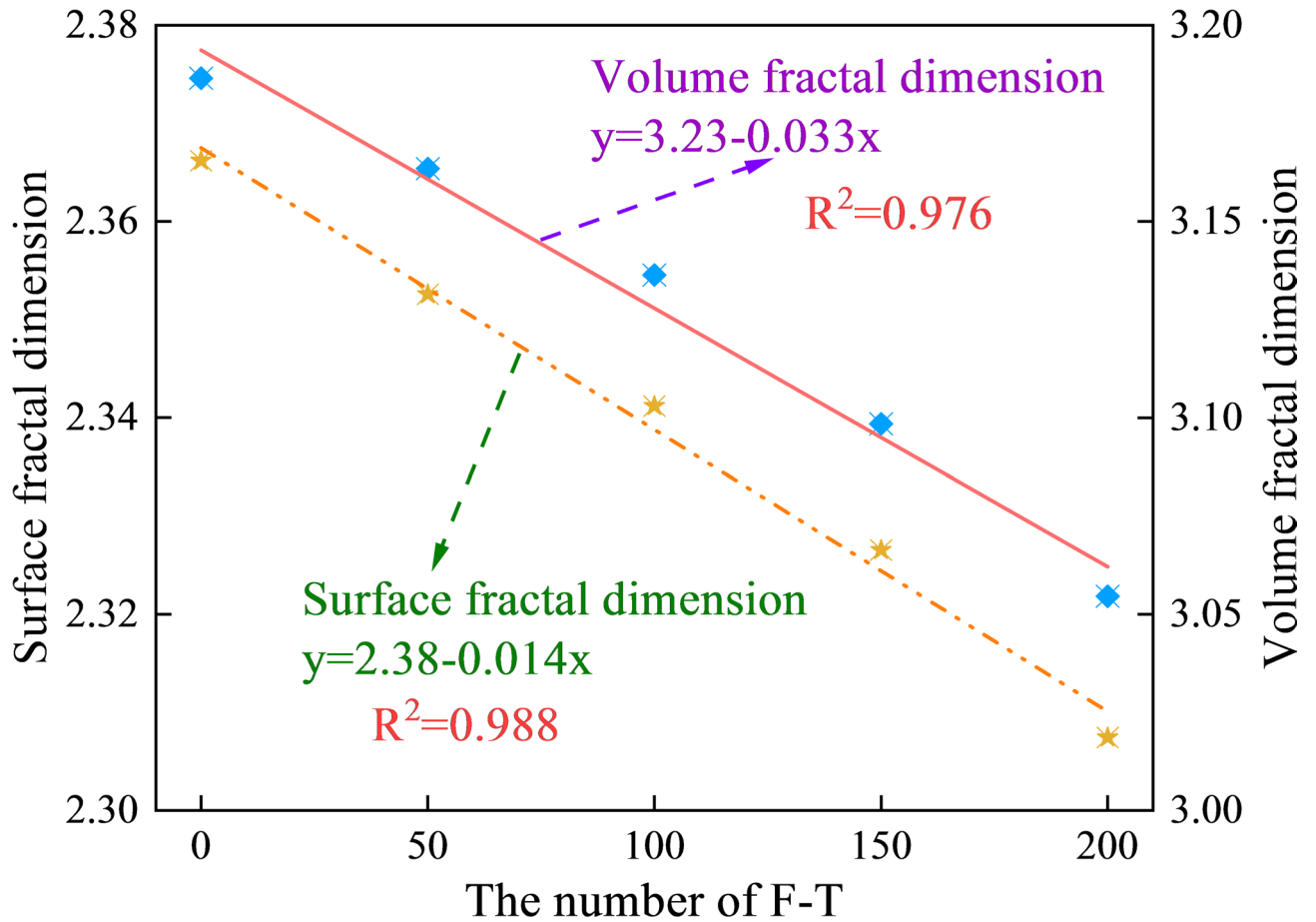


Fig. 9. Surface fractal dimension and volume fractal dimension of SCC pores under different F-T cycles.

where, D is the damage variable; \tilde{A} is the effective bearing area; A is the total carrying area. The boundary conditions are:

$$D = \begin{cases} 0, & \tilde{A} = A \\ 1, & \tilde{A} = 0 \end{cases} \quad (2)$$

According to hydrostatic pressure hypothesis and osmotic pressure hypothesis of Powers, the essence of F-T damage is the change of pore structure of materials. In order to describe the F-T damage of SCC more effectively and conveniently, the effective bearing area and total bearing area were replaced by the fractal dimension of state of no F-T and after F-T damage respectively through the transformation function based on the correlation between the fractal dimension and F-T cycles. This method has been proved by Liu, et al. in Reference⁵⁶. Therefore, the F-T damage degree based on the fractal dimension is:

$$D = 1 - \frac{F_t - F_{min}}{F_0 - F_{min}} \quad (3)$$

where F_t is the fractal dimension after F-T times; F_0 is the fractal dimension before F-T; F_{min} is the theoretical minimum value of fractal dimension, which is 2 in this case.

At this point, the boundary condition changes to:

$$D = \begin{cases} 0, & F_t = F_0 \\ 1, & F_t = F_{min} \end{cases} \quad (4)$$

According to the above steps, the F-T damage degree of the surface fractal and the volume fractal of the SCC pores were calculated respectively, and the results are shown in Fig. 10.

Figure 10 shows the calculation results of the F-T damage degree of SCC based on fractal dimension under 0, 50, 100, 150, and 200 F-T cycles. It can be seen from the figure that the F-T damage degree calculated from the surface fractal dimension and volume fractal dimension presents an upward trend with the increase in F-T cycles. This is consistent with our conventional understanding of F-T damage. In addition, it can also be seen from the

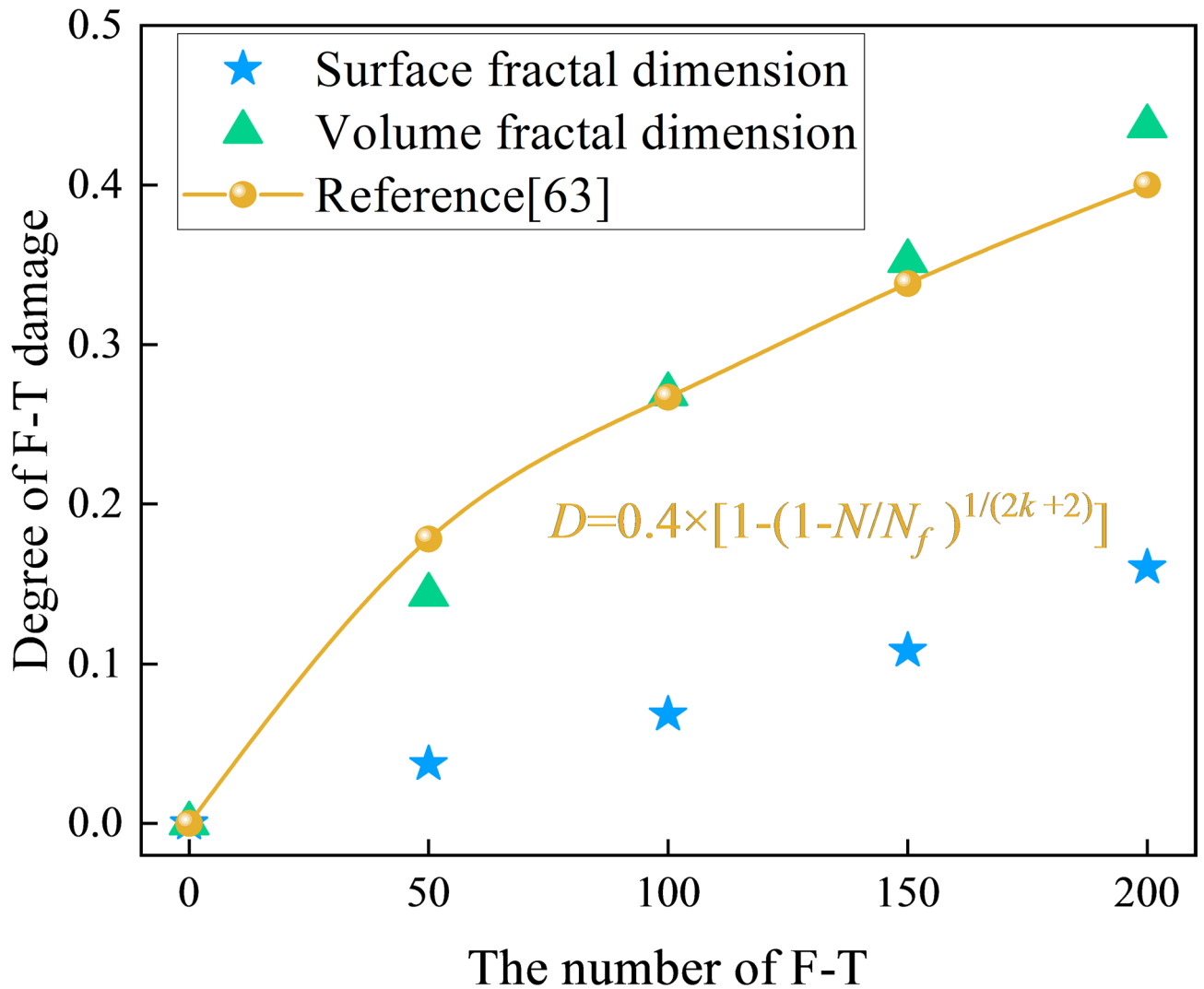


Fig. 10. F-T damage degree of SCC. Note N and N_f represent the number of F-T and the critical number of F-T, respectively, and k is a material constant with a value of -0.1427 .

figure that the F-T damage degree ranges of the surface fractal dimension and volume fractal dimension are from 0 to 0.16 and 0 to 0.44, respectively. It can be seen that the F-T damage degree obtained by the two calculation methods is very different. In order to select a more reasonable calculation method of F-T damage degree, the F-T damage model in Bai et al.⁶³ was introduced (Fig. 10). It can be seen that the development trend of the volume fractal dimension is basically consistent with that of the F-T damage model, and some feature points overlap. To this end, Pearson correlation tests were performed on the volume fractal dimension and the F-T damage model using the two-tailed significance test under the significance level of 0.05 and confidence interval of 95%. The test results show that the value of the Pearson product moment correlation coefficient is 0.993. This indicates that the F-T damage degree of the volume fractal dimension is highly correlated with the F-T damage model in Bai et al.⁶³. However, the results of the F-T damage degree calculated based on the surface fractal dimension were relatively small, which is in sharp contrast to the results of the volume fractal dimension.

Conclusion

This study focused on the performance changes of SCC in the F-T environment, aiming to accurately quantify and reveal the changes of its surface and pore structure during the F-T cycles, so as to achieve an effective assessment of the F-T damage of SCC. The main conclusions are as follows:

- (1) The surface of SCC tends to gradually deteriorate with the increase in F-T cycles. The point cloud data of the SCC surface fluctuated in different amplitudes caused by F-T cycles, and the ranges were 0–0.15 mm, 0–0.36 mm, 0–0.54 mm, 0–0.77 mm, and 0–0.93 mm, respectively. Surface roughness was used to describe the F-T damage to the surface of SCC, and it was found that the surface roughness of SCC was 0.097, 0.137, 0.226, 0.383, and 0.899 mm under different F-T cycles, respectively, and its development trends accord with the Exp3P2 model and basically follow the exponential growth law.

- (2) The pore size and porosity of SCC increased with the increase in F-T cycles, and the growth rates of pore size and porosity were 3.41%, 12.90%, 18.68%, 19.69% and 33.86%, 41.85%, 30.26%, 29.29%, respectively. However, the number of pores decreased by 5.86%, 2.56%, 11.00%, and 11.56%, respectively. The F-T damage of SCC was evaluated based on the surface fractal dimension and volume fractal dimension of the pore structure, and the ranges of F-T damage were obtained as approximately 0–0.16 and 0–0.44, respectively. The volume fractal dimension is more suitable for characterizing the F-T damage degree of SCC than the surface fractal dimension.
- (3) This study systematically investigated the changes in the surface and pore structure of SCC during the F-T cycle, but there are still some limitations. The conditions set for the F-T cycles in the experiments were relatively idealized; in actual engineering, the environment in which SCC is situated is more complex and may be simultaneously affected by various factors beyond F-T cycles (such as salt erosion, load effects, etc.). This study did not fully consider the impact of these multi-factor coupling effects on the performance of SCC. In the future, we will simulate a complex environment that is closer to the actual working conditions, conduct research on the performance of SCC under the combined action of F-T cycles and other factors (such as salt solution erosion, mechanical loads, etc.), and deeply reveal the influence mechanism of multi-factor coupling on the durability of SCC.

Data availability

The datasets used and/or analysed during the current study available from the corresponding author on reasonable request.

Received: 15 March 2025; Accepted: 11 June 2025

Published online: 02 July 2025

References

1. Xiao, J. et al. A numerical and theoretical analysis of the structural performance for a new type of steel-concrete composite aqueduct. *Eng. Struct.* **245**, 112839 (2021).
2. Lv, C. Application of assembly technology of green intelligent manufacturing and harmonious development in water conservancy construction. *China Water Resour.* **01**, 65–67 (2020).
3. Mostafavi, S. A. & Joneidi, Z. Thermal model of precast concrete curing process: Minimizing energy consumption. *Math. Math. Comput. Simul.* **191**, 82–94 (2022).
4. Yunfeng Qian, D. et al. Development of cementless alkali-activated ultra-high performance concrete under various steam curing regimes: Mechanical properties, permeability, and microstructure. *J. Build. Eng.* **101**, 111857 (2025).
5. Subhash, C. et al. Influence of curing regimes and duration on the early strength development of fibers based reactive powder concretes. *J. Build. Eng.* **102**, 112020 (2025).
6. Chen, B. et al. Experimental study on compressive strength and Frost resistance of steam cured concrete with mineral admixtures. *Constr. Build. Mater.* **325**, 126725 (2022).
7. Yu, Y. et al. Evolution of temperature stress and tensile properties of concrete during steam-curing process. *Constr. Build. Mater.* **305**, 124691 (2021).
8. Shi, J. et al. Heat damage of concrete surfaces under steam curing and improvement measures. *Constr. Build. Mater.* **252**, 119104 (2020).
9. Chen, G. et al. Comparative study on mechanical properties and microstructure development of ultra-high performance concrete incorporating phosphorous slag under different curing regimes. *Constr. Build. Mater.* **392**, 131963 (2023).
10. Ma, F. et al. Analysis of damage models and mechanisms of mechanical sand concrete under composite salt freeze-thaw cycles. *Constr. Build. Mater.* **429**, 136311 (2024).
11. Soner & Guler Zehra Funda Akbulut. A comprehensive review of concrete durability in freeze-thaw conditions: Mechanisms, prevention, and mitigation strategies. *Structures* **75**, 108804. (2025).
12. henhua, S. & Scherer, G. W. Effect of air voids on salt scaling and internal freezing. *Cem. Concr. Res.* **40**, 260–270 (2010).
13. Kheradmandi, N. & Radenberg, M. Employing 3D laser scanner for automated morphological assessment of aggregates produced from diverse sources and by different crushing methods. *Constr. Build. Mater.* **448**, 138034 (2024).
14. Mertens, B. & Delchambre, A. 3D reconstruction: Why should the accuracy always be presented in the pixel unit? *Image Vis. Comput.* **48–49**, 57–60. (2016).
15. Yuan, P. F. et al. Real-time toolpath planning and extrusion control (RTPEC) method for variable-width 3D concrete printing. *J. Build. Eng.* **46**, 103716 (2022).
16. Wang, X. et al. Optimization of 3D printing concrete with coarse aggregate via proper mix design and printing process. *J. Build. Eng.* **56**, 104745 (2022).
17. Souza, M. T. et al. 3D printed concrete for large-scale buildings: An overview of rheology, printing parameters, chemical admixtures, reinforcements, and economic and environmental prospects. *J. Build. Eng.* **32**, 101833 (2020).
18. Chao Liu, H. et al. Effect of X-ray CT characterized pore structure on the freeze-thaw resistance of 3D printed concrete with recycled coarse aggregate. *Constr. Build. Mater.* **469**, 140492 (2025).
19. Hoła, J. et al. Usefulness of 3D surface roughness parameters for nondestructive evaluation of pull-off adhesion of concrete layers. *Constr. Build. Mater.* **84**, 111–120 (2015).
20. Sarker, M., Dias-da-Costa, D. & Hadigheh, S. A. Multi-scale 3D roughness quantification of concrete interfaces and pavement surfaces with a single-camera set-up. *Constr. Build. Mater.* **222**, 511–521 (2019).
21. Cho, S. et al. Foam stability of 3D printable foamed concrete. *J. Build. Eng.* **47**, 103884 (2022).
22. Gan, L. et al. Investigation on the evolution of concrete pore structure under freeze-thaw and fatigue loads. *J. Build. Eng.* **97**, 110914 (2024).
23. Daguang Huang, X. et al. Advanced nuclear magnetic resonance technology analysis of hybrid fiber reinforced concrete for optimized pore structure and strength. *Constr. Build. Mater.* **467**, 140383 (2025).
24. Han, X., Wang, B. & Feng, J. Relationship between fractal feature and compressive strength of concrete based on MIP. *Constr. Build. Mater.* **322**, 126504 (2022).
25. Khonsari, S. V., Eslami, E. & Anvari, A. Fibrous and non-fibrous perlite concretes—experimental and SEM studies. *Eur. J. Environ. Civ. Eng.* **22**, 138–164 (2018).
26. Mundra, S., Agrawal, V. & Nagar, R. Sandstone cutting waste as partial replacement of fine aggregates in concrete: A mechanical strength perspective. *J. Build. Eng.* **32**, 101534 (2020).

27. Sokhansefat, G. et al. Using X-ray computed tomography to investigate mortar subjected to freeze-thaw cycles. *Cem. Concrete Compos.* **108**, 103520 (2020).
28. Tian, W. & Han, N. Pore characteristics (>0.1 mm) of non-air entrained concrete destroyed by freeze-thaw cycles based on CT scanning and 3D printing. *Cold Reg. Sci. Technol.* **151**, 314–322 (2018).
29. Yang, S., Cui, H. & Poon, C. S. Assessment of in-situ alkali-silica reaction (ASR) development of glass aggregate concrete prepared with dry-mix and conventional wet-mix methods by X-ray computed micro-tomography. *Cem. Concr. Compos.* **90**, 266–276 (2018).
30. Zhao, D. et al. Study on the correlation between pore structure characterization and early mechanical properties of foamed concrete based on X-CT. *Constr. Build. Mater.* **450**, 138603 (2024).
31. Zou, C. et al. Evolution of multi-scale pore structure of concrete during steam-curing process. *Microporous Mesoporous Mater.* **288**, 109566 (2019).
32. Jiao, Z., Li, X. & Yu, Q. Effect of curing conditions on freeze-thaw resistance of geopolymers containing various calcium resources. *Constr. Build. Mater.* **313**, 125507 (2021).
33. Lv, Q. et al. Fractal dimension of concrete incorporating silica fume and its correlations to pore structure, strength and permeability. *Constr. Build. Mater.* **228**, 116986 (2019).
34. GB/T 50082–2024. *Standard for Test Method of long-term Performance and Durability of Ordinary Concrete* (Academy of Building Research, 2024).
35. ASTM C666. *Standard Test Method for Resistance of Concrete To Rapid Freezing and Thawing* (West Conshohocken, 2011).
36. Mirzaei, K. et al. 3D point cloud data processing with machine learning for construction and infrastructure applications: A comprehensive review. *Adv. Eng. Inf.* **51**, 101501 (2022).
37. Wu, Z. et al. High-volume point cloud data simplification based on decomposed graph filtering. *Autom. Constr.* **129**, 103815 (2021).
38. Asad Ur Rahman, Vedhus Hoskere. Instance segmentation of reinforced concrete Bridge point clouds with Transformers trained exclusively on synthetic data. *Autom. Constr.* **173**, 106067 (2025).
39. Li, L. Xuping, Z. A robust assessment method of point cloud quality for enhancing 3D robotic scanning. *Robot. Comput.-Integr. Manuf.* **92**, 102863. (2025).
40. Elhoseny, M. & Shankar, K. Optimal bilateral filter and convolutional neural network based denoising method of medical image measurements. *Measurement* **143**, 125–135 (2019).
41. Xiao, J. et al. Application of density clustering and PCA point cloud data processing in high-speed rail track detection. *Railw. Stand. Des.* **64**, 37–42 (2020).
42. Luo, H. et al. A robust method for multi-view 3D data Stitching based on pasted marked points. *Measurement* **228**, 114364 (2024).
43. Wang, C. et al. Review of hole repair in point cloud model. *Mod. J. Manuf. Sci. Eng.* **09**, 156–162 (2020).
44. Liu, Z. et al. Investigation on micro-structure of self-compacting concrete modified by recycled grinded tire rubber based on X-ray computed tomography technology. *J. Clean. Prod.* **290**, 125838 (2021).
45. Sarkar, S., Wahi, P. & Munshi, P. *An Empirical Correction Method for beam-hardening Artifact in Computerized Tomography (CT) Images* 102104–113 (NDT & E International, 2019).
46. Guo, Y. et al. Analysis of foamed concrete pore structure of railway roadbed based on X-ray computed tomography. *Constr. Build. Mater.* **273**, 121773 (2021).
47. Santos, P. M. D. & Júlio, E. N.B.S. A state-of-the-art review on roughness quantification methods for concrete surfaces. *Constr. Build. Mater.* **38**, 912–923 (2013).
48. Chen Xing, B. et al. Research on the roughness characteristics of cement concrete base after treatment based on 3D laser detection technology. *Constr. Build. Mater.* **460**, 139818 (2025).
49. Dong, Y. et al. Microstructural damage evolution and its effect on fracture behavior of concrete subjected to freeze-thaw cycles. *Int. J. Damag. Mech.* **27**, 1272–1288 (2018).
50. SL/T 352– Test code for hydraulic concrete. Ministry of Water Resources of the People's Republic of China: Beijing, China (2020).
51. Li, D. et al. Fractal characteristics of pore structure of hybrid Basalt–Polypropylene fibre-reinforced concrete. *Cem. Concr. Compos.* **109**, 103555 (2020).
52. Du, W., Liu, Q. & Lin, R. Effects of toluene-di-isocyanate microcapsules on the Frost resistance and self-repairing capability of concrete under freeze-thaw cycles. *J. Build. Eng.* **44**, 102880 (2021).
53. Wei, Y. et al. Correlation between mechanical properties and pore structure deterioration of recycled concrete under sulfate freeze-thaw cycles: An experimental study. *Constr. Build. Mater.* **412**, 134794 (2024).
54. Gao, D. et al. Compressive behavior of GFRP partially strengthened corroded RC columns subjected to freeze-thaw erosion. *J. Build. Eng.* **57**, 104883 (2022).
55. Li, F., Luo, D. & Niu, D. Durability evaluation of concrete structure under freeze-thaw environment based on pore evolution derived from deep learning. *Constr. Build. Mater.* **467**, 140422 (2025).
56. Liu, Y. et al. Structural performance assessment of concrete components based on fractal information of cracks. *J. Build. Eng.* **43**, 103177 (2021).
57. Hao, J., Qiao, L. & Li, Q. Study on cross-scale pores fractal characteristics of granite after high temperature and rock failure precursor under uniaxial compression. *Powder Technol.* **401**, 117330 (2022).
58. Jin, S., Zheng, G. & Yu, J. A micro freeze-thaw damage model of concrete with fractal dimension. *Constr. Build. Mater.* **257**, 119434 (2020).
59. Sun, D. Method for Non-destructive testing of the surface fractal dimension of foam concrete. *New. Build. Mater.* **51** (06), 166–170 (2024).
60. Zhang Wei, L. et al. Degradation mechanism of Freeze-Thaw damage of rice husk Ash concrete based on pore volume fractal dimension. *J. Compos. Mater.* **40** (08), 4733–4744 (2023).
61. Lemaitre, J. How to use damage mechanics. *Nucl. Eng. Des.* **80**, 233–245 (1984).
62. Kochanov, D. Time of rupture process under creep conditions. *Izv. Akademii Nauk. Sssr-Seriya Khimicheskaya* 26–31. (1958).
63. Bai, J. et al. Damage degradation model of aeolian sand concrete under freeze–thaw cycles based on macro-microscopic perspective. *Constr. Build. Mater.* **327**, 126885 (2022).

Author contributions

C.J.(Jialin Chen) conceptualized the research idea and wrote the main manuscript text.H.Z.(Zhifan He): Writing – review & editing, Writing – original draft, Software, Methodology, Formal analysis, Data curation. C.K.(Shoukai Chen): Visualization, Validation, Supervision, Resources, Project administration.N.P.(Phu Minh Vuong Nguyen): Validation, Resources, Methodology, Formal analysis.L.J.(Jinping Liu): Validation, Investigation, Formal analysis. X.H.(Haokai Xu): Validation, Investigation.All authors reviewed and approved the final version of the manuscript.

Declarations

Competing interests

The authors declare no competing interests.

Additional information

Correspondence and requests for materials should be addressed to S.C.

Reprints and permissions information is available at www.nature.com/reprints.

Publisher's note Springer Nature remains neutral with regard to jurisdictional claims in published maps and institutional affiliations.

Open Access This article is licensed under a Creative Commons Attribution-NonCommercial-NoDerivatives 4.0 International License, which permits any non-commercial use, sharing, distribution and reproduction in any medium or format, as long as you give appropriate credit to the original author(s) and the source, provide a link to the Creative Commons licence, and indicate if you modified the licensed material. You do not have permission under this licence to share adapted material derived from this article or parts of it. The images or other third party material in this article are included in the article's Creative Commons licence, unless indicated otherwise in a credit line to the material. If material is not included in the article's Creative Commons licence and your intended use is not permitted by statutory regulation or exceeds the permitted use, you will need to obtain permission directly from the copyright holder. To view a copy of this licence, visit <http://creativecommons.org/licenses/by-nc-nd/4.0/>.

© The Author(s) 2025